Dynamical simulations of single-mode lasing in large-area all-semiconductor PCSELs

Mindaugas Radziunas[1], Hans Wenzel[2], Ben King[2], Paul Crump[2], Eduard Kuhn[1]

[1] Weierstrass Institute
Mohrenstraße 39
10117 Berlin
Germany
E-Mail: mindaugas.radziunas@wias-berlin.de
eduard.kuhn@wias-berlin.de

[2] Ferdinand-Braun-Institut
Leibniz Institut für Höchstfrequenztechnik
Gustav-Kirchhoff-Straße 4
12489 Berlin
Germany
E-Mail: hans.wenzel@fbh-berlin.de
ben.king@fbh-berlin.de
paul.crump@fbh-berlin.de

Dynamical simulations of single-mode lasing in large-area all-semiconductor PCSELs

Mindaugas Radziunas, Hans Wenzel, Ben King, Paul Crump, Eduard Kuhn

Abstract

We perform modeling and dynamic simulations of all-semiconductor photonic crystal surface-emitting lasers (PCSELs). A two-dimensional photonic crystal consists of a GaAs layer with InGaP features, repeating periodically in both lateral directions. In our dynamic simulations, we demonstrate for the first time that photonic crystals with large isosceles triangular features, having a base angle close to $71.5°$, enable suppression of higher-order modes and achieve single-mode, high-quality lasing in large-area all-semiconductor PCSELs under moderate and even high pump levels.

Photonic crystal (PC) surface-emitting lasers (SELs) are devices engineered to achieve single-mode operation and a narrow far-field emission pattern by utilizing a photonic crystal structure [1, 2]. Unlike existing high-power PCSELs, which feature a PC layer composed of periodically arranged air voids [1, 2], this letter investigates the potential of employing all-semiconductor PC layers, which could be beneficial for enhancing the efficiency and manufacturabillity of PCSELs. The refractive index contrast between the two materials in these PC layers is significantly lower than that in semiconductor/air-void PCs. As a result, the coupling of counter- and cross-propagating fields in all-semiconductor PCs is relatively weak. However, it can still be effectively harnessed in large-area devices, where it enables large field intensities in the central region of the PC layer, with only minimal field losses at the lateral edges of the domain. We also aim to use large PC features that are adequately separated from one another, with fill factors $f = A_{\mathrm{f}}/a^2$ close to 0.5 providing large coupling to the vertical field. Here, a is the lattice constant (the edge length of the square unit cell) and A_{f} is the area of the feature. While large values of f are expected to enhance field coupling, manufacturing processes requires sufficient separation between neighboring features. Given these requirements, employing dual-lattice PCs defined by a pair of similar, non-overlapping features shifted by $a\sqrt{2}/4$ along the diagonal of the unit cell, as explored in the best semiconductor/air-void PCSELs [3, 4], is hardly possible in all-semiconductor PCSELs due to the reduced vertical field coupling. The use of right-angle isosceles triangular features (RIT), as suggested in pioneering works on PCSELs [5], leads to a pronounced coupling of counter-propagating fields and results in only a modest suppression of higher-order modes in large all-semiconductor cold-cavity PCSELs [6, 7]. This suppression may be insufficient when operating these PCSELs under high-pumping conditions, as it is compromised by carrier spatial hole burning (SHB) [4] and heating-induced changes in the model parameters, particularly when the PCSEL is operating in continuous-wave (cw) mode. In our theoretical work [8], we proposed using stretched isosceles triangles (SIT), which are symmetric with respect to the diagonal of the PC unit cell, have a base angle close to $\arctan 3 \sim 71.5°$, and $f \approx 3/8$. Mode calculations conducted for cold-cavity, finite-sized PCSELs in [8] indicated that the higher-order mode gain discrimination ΔG in PCSELs with SIT features can exceed $10\,\mathrm{cm}^{-1}$ for devices of size $L = 1\,\mathrm{mm}$ and remain as high as $1\,\mathrm{cm}^{-1}$ for $3\,\mathrm{mm}$ devices. Here, the size factor L defines the dimensions of the PCSEL in both lateral directions for a $L \times L$ square cavity. The improved mode discrimination at large L is achieved by weakening the 1D Hermitian coupling strength, which leads to increased losses at the edge of the finite-size device, which

are disproportionately large for higher-order modes. In this letter, we investigate the above-threshold behaviour of large all-semiconductor PCSELs utilizing either RIT or SIT features within the PC layer, while maintaining the same vertical structure of the PCSEL itself. Our results demonstrate that, at higher bias currents, the expected operation of RIT-PCSELs is characterized by multiple modes, leading to degradation in the quality of emission. In contrast, SIT-PCSELs can maintain strong side-mode suppression and emit a high-quality beam characterized by single-mode operation, even at elevated bias levels.

The above-threshold behaviour of PCSELs is simulated using a dynamical model based on a three-dimensional coupled-wave theory [5, 9]. Similarly to [9], the field equations are represented by a system of four linear PDEs in one temporal and two spatial dimensions, within the in-plane domain $Q_{\mathrm{L}} = [0, L] \times [0, L]$:

$$
\begin{aligned}
&\tfrac{1}{v_{\mathrm{g}}} \partial_t \mathbf{E}(x, y, t) = \big[\mathbf{D} + i(\mathbf{C} - \Delta\beta(N)) \big] \mathbf{E} + \mathbf{F}_{\mathrm{sp}}, \\
&E_1(0, y, t) = E_2(L, y, t) = E_3(x, 0, t) = E_4(x, L, t) = 0, \\
&\mathbf{D} = \begin{pmatrix} \sigma\partial_x & 0 \\ 0 & \sigma\partial_y \end{pmatrix}, \quad \sigma = \begin{pmatrix} -1 & 0 \\ 0 & 1 \end{pmatrix}.
\end{aligned}
\tag{1}
$$

The 4-component complex field function $\mathbf{E}$ consists of the complex, slowly-varying amplitudes of counter-propagating fields along the x- and y-directions, represented by (E_1, E_2) and (E_3, E_4), respectively. The four field components satisfy non-reflecting boundary conditions at the edges of Q_{L}, which implies that all fields exiting Q_{L} are fully lost beyond the domain boundaries. v_{g} in (1) is the group velocity, derived according to [7], $\mathbf{F}_{\mathrm{sp}}$ represents spontaneous emission [7, 10], while $\mathbf{C}$ is a complex (4×4)-field coupling matrix, introduced in, e.g., [5, 9], efficiently estimated using analytical expression-based algorithms [6, 11]. It depends on the shape and fill factor of the PC feature as well as the vertical structure of the entire PCSEL. Finally, $\Delta\beta$ is a spatially-distributed relative propagation factor,

$$
\Delta\beta(N) = k_0 \Delta_n(N) + \tfrac{i}{2}[g(N) - \alpha] - i\mathcal{D}.
\tag{2}
$$

It accounts for the carrier-dependent logarithmic gain $g(N)$, the square-root-like refractive index change $\Delta_n(N)$, and the total field loss α, which includes the scattering loss, the modal waveguide absorption, and the (linear with N) free-carrier absorption in the active layer [7]. $k_0 = 2\pi/\lambda_0$ is the central wavevector, ($\lambda_0 = a n_{\mathrm{eff}}$: central wavelength, n_{eff}: effective refractive index). Linear operator $\mathcal{D}$ models Lorentzian-shaped gain dispersion and can be realized by a set of ODE's [12]. During simulations, the action of (discretized) $\mathcal{D}$ can also be interpreted as an infinite impulse response digital filter, which aids our numerical schemes by smoothing out small discontinuities that may otherwise arise and persist in hyperbolic PDEs. Possible parameter dependencies on temperature [13] leading to thermal lensing, e.g., are neglected in this study.

As in [9, 10], the dynamics of the spatially distributed carrier density $N(x, y, t)$ is governed by a diffusive carrier rate equation

$$
\begin{aligned}
&\partial_t N = \nabla_\perp \cdot (D_N \nabla_\perp) N + \tfrac{j}{ed} - R_{\mathrm{sp}}(N) - R_{\mathrm{st}}(N, \mathbf{E}), \\
&R_{\mathrm{sp}} = \tfrac{N}{\tau_N} + BN^2 + CN^3, \quad R_{\mathrm{st}} \propto \Re[\mathbf{E}^* \cdot (g(N) - 2\mathcal{D})\mathbf{E}].
\end{aligned}
\tag{3}
$$

Here, $\nabla_\perp = \begin{pmatrix} \partial_x \\ \partial_y \end{pmatrix}$, e is the elementary charge, d is the thickness of the active zone (AZ), and $(\cdot)$ denotes the standard dot product of two vectors. The proportionality coefficient in the stimulated recombination term R_{st} depends on the normalization of the field function $\mathbf{E}$, v_{g}, d, n_{eff}, and the refractive index n_{AZ} in the AZ [7, 9]. In contrast to [9, 10], our rate equation (3) incorporates cubic spontaneous recombination R_{sp} (with τ_N representing the carrier lifetime due to Shockley–Read–Hall recombination, and B and C denoting the spontaneous radiative and Auger recombination coefficients), spatially

distributed carrier diffusion $D_N = \mu_p(p_0 + N)\partial_N\phi_F(N)$. Here, μ_p, p_0, and ρ are the mobility of holes in the AZ, their equilibrium density, and conductivity, respectively [14]. To determine the bias current density $j(x, y, t) = (\rho\partial_z\phi_p)|_{z=\text{AZ}}$ in the AZ, we solve the Laplace equation $\nabla \cdot (\rho(x, y, z)\nabla)\phi_p = 0$ for the quasi-Fermi potential ϕ_p in the three-dimensional p-doped region Q_{CS}. This involves using the Fermi voltage $\phi_F(N)$ at the interface to the active zone (AZ) (estimated at actual N according to the Unger approximation [15]), the applied voltage U at the contact, and homogeneous Neumann conditions at the remaining boundaries of Q_{CS}. Since the problem is linear, the major computations can be performed in advance for a set of elementary boundary conditions. The required j is then generated as a linear combination of these elementary solutions for each actual distribution of N obtained during the time-domain calculations [16]. In contrast to the fixed distribution j typically used in carrier rate equations, our approach provides a more accurate description of inhomogeneous current spreading and accounts for bias readjustments when the SHB of carriers is well pronounced [14]. In the following examples, we used the parameters $\lambda_0 = 1.07\,\mu\text{m}$, $\mu_p = 2.788 \times 10^6\,\text{m}^2/\text{Vs}$, $p_0 = 1.47 \times 10^7\,\text{m}^{-3}$, $c/v_\text{g} = 3.782$. Other parameters and the vertical structure of the device are as in [7]. Unlike in [8], this structure does not include a distributed Bragg reflector (DBR), avoiding the need for additional adjustments to the field phase at the DBR. As a result, approximately equal power is expected at both the top and bottom surfaces of the simulated PCSEL.

Before simulating the dynamics in PCSELs, we first calculate the spectra of the field equations (1), which are linear with respect to $\mathbf{E}$ when the distribution of $\Delta\beta$ is fixed. By setting $\Delta\beta = 0$, neglecting $\mathbf{F}_{\text{sp}}$, and assuming $\mathbf{E} = \mathbf{\Theta}(x, y)e^{i\Omega t}$ in (1), we obtain a spectral problem for the vector-eigenfunctions $\mathbf{\Theta}$ and the complex eigenfrequencies Ω. We solve this problem on a reduced domain $Q_\text{c} \subset Q_\text{L}$, which corresponds to the contact region with an area of $|Q_\text{c}| = L_\text{c}^2$. Here, L_c represents the side length of the square contact considered in this work. The blue dots in Fig. 1(b) represent most important Ω, calculated for a finite-size PCSEL with a PC layer defined by RIT features with the base $0.8\sqrt{2}a$, see panel (a). $\Re\Omega$ is the relative frequency of the corresponding mode, and $\Delta\lambda = \frac{-\lambda_0^2\Re\Omega}{2\pi c_0}$ is the mode's
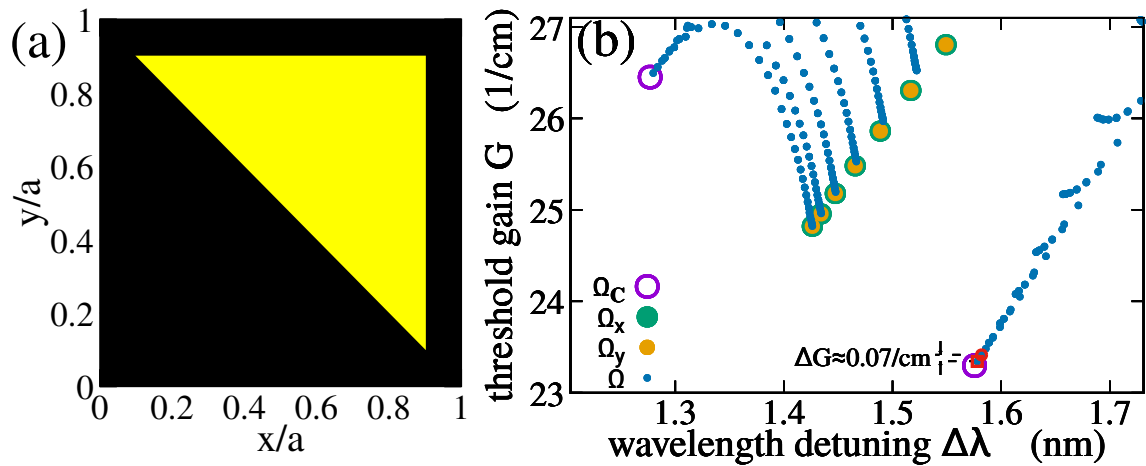

Figure 1: (a): RIT feature in the unit cell of the PC. (b): Eigenfrequencies of the spectral problem with $\Delta\beta = 0$ in the square Q_c with $L_\text{c} = 1.6\,\text{mm}$ (blue), same device with ignored cross-coupling terms of $\mathbf{C}$ (green/orange), and of $\mathbf{C}$ alone (magenta). Red box/circle: fundamental/first higher order mode.

wavelength detuning from λ_0. $G = 2\Im\Omega/v_\text{g}$ determines the mode's threshold gain, or more precisely, the spatial average of $g(N) - \alpha$ that must be reached for the mode to begin lasing. Notably, in a well-pumped PCSEL, the distributions of N and $g(N)$ have their highest values within the lateral contact region Q_c. This must be considered when estimating the threshold current $I_{\text{th}} \approx ed|Q_\text{c}|R_{\text{sp}}(N_{\text{th}})$. The constant N_{th} is determined from the equation $v_\text{g}(g(N_{\text{th}}) - \alpha) = 2\Im\Omega_0$, where Ω_0 is the fun-

damental mode frequency, calculated using the reduced PCSEL area Q_c. In addition to the main eigenvalues, Fig. 1(b) displays two (of the four) lowest-threshold eigenfrequencies $\Omega_{\mathbf{C}}$ of the complex matrix $\mathbf{C}$, which serve as accumulation points for complex Ω in large-area PCSELs. The gain threshold for the fundamental mode (a red box in Fig. 1(b)) in the finite-size PCSEL under consideration is already approaching that of $\Omega_{\mathbf{C}0}$, which is the eigenfrequency of $\mathbf{C}$ with the smallest imaginary part. Therefore, increasing the PCSEL area results only a minor decrease in the threshold gain, but further reduces the already small gain gap, ΔG, between the fundamental mode and the first higher-order mode (a red circle in the same figure). Besides the modes converging toward $\Omega_{\mathbf{C}0}$ (large empty bullet at $\Delta\lambda \approx 1.57\,\mathrm{nm}$), many other higher-order modes are essentially one-dimensional. These cluster at the green and orange bullets, representing modes of a related problem where the coupling of cross-propagating field components (off-diagonal 2×2 matrix blocks of $\mathbf{C}$) has been intentionally excluded [11].
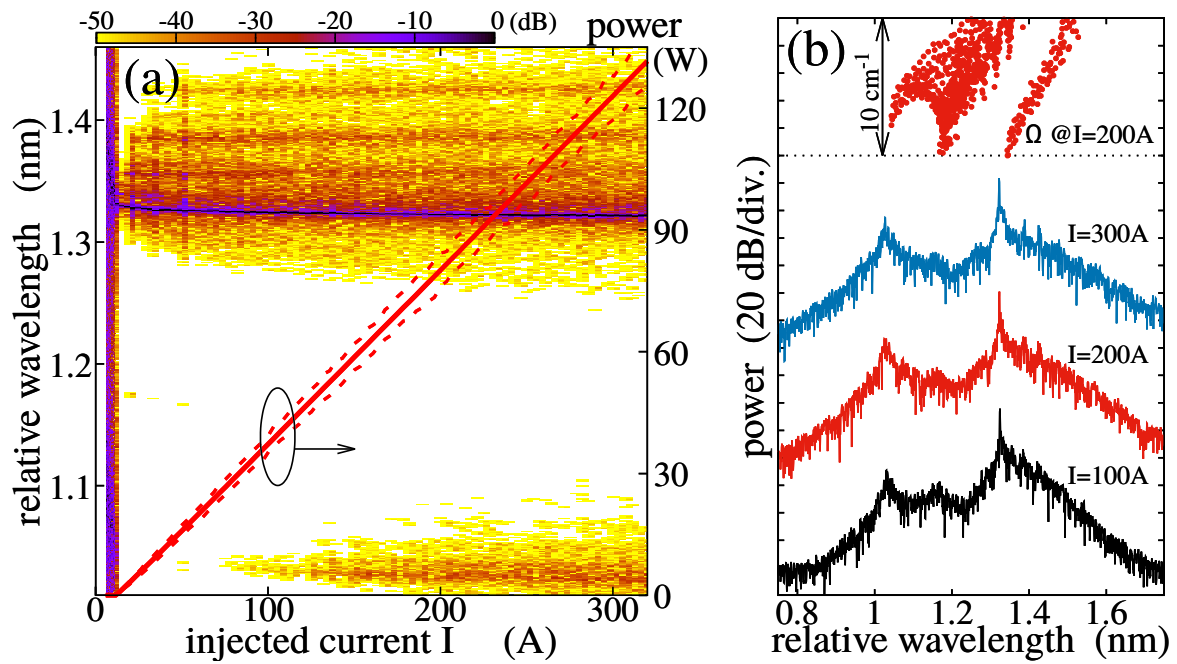

Figure 2: (a): Mapping of normalized optical spectra (color-coded on a log scale) and the mean, minimum, and maximum emitted beam power at the n-doped side (solid and dashed red lines) as functions of the total bias current I in the $L = 2\,\mathrm{mm}$ RIT-feature-based PCSEL with $L_c = 1.6\,\mathrm{mm}$. Only spectral peaks with suppression $\leq 50\,\mathrm{dB}$ are shown. (b): Optical spectra for selected I, offset by 80 dB for clarity. Dots: relative wavelengths and damping of modes at 200 A.

Next, we performed simulations of the dynamical PCSEL model (1-3) for a series of up-tuned voltages U. For each given voltage, we simulated 10 ns-long transients and evaluated the bias current I, emission intensity, and optical spectra at one (n-doped side) vertical edge of the PCSEL using the second half of each transient. The results for a $L = 2\,\mathrm{mm}$ RIT-based PCSEL with a $L_c = 1.6\,\mathrm{mm}$-large contact are shown in Fig. 2. Notably, due to the minimal gain discrimination between the fundamental and higher-order modes, single-mode lasing was observed only very close to the threshold. At higher currents, single-mode operation was lost, as evidenced by the noticeable separation between the minimum and maximum emitted beam intensities (thin dashed lines in panel (a)) and the broadening of the optical spectrum around the main peak (depicted by the dark colors in the same panel). Typical broadened spectra for $I = 100, 200$, and $300\,\mathrm{A}$ are displayed in panel (b) of the same figure. Strong and broad spectral lines correspond to the wavelengths $\Delta\lambda$ of multiple closely-spaced low-$\Im\Omega$

modes, indicated by dots in the upper part of panel (b), calculated for $I = 200$ A. A blue $\Delta\lambda$-shift in these hot-cavity modes compared to the cold-cavity modes in Fig. 1(b) arises from the refractive index change function $\Delta_n(N)$. The bias current-induced nonuniformity of $\Delta\beta$ implies further perturbations of the relevant complex mode frequencies Ω.

Due to the weak refractive index contrast in the all-semiconductor PC layer, the magnitude of the 1D-coupling elements in $\mathbf{C}$ (which provide direct coupling between E_1 with E_2 and E_3 with E_4) is an order of magnitude larger than that of any other 2D-coupling elements in this matrix. In similar PCSELs with semiconductor-air-based PC layers, this ratio is approximately three. This significant difference complicates the manipulation of $\Im\Omega_{\mathbf{C}}$ while maintaining adequate mode gain discrimination when utilizing similar RIT-shaped and most other isosceles triangular features of the PC [8]. The primary contribution to the 1D coupling in these triangular-feature-based PCSELs arises from the strong direct coupling of the fundamental counterpropagating waves, resulting in large elements in the 1D coupling submatrix $\mathbf{C}_{1D}$ defined in, for example, [5, 9]. It has been demonstrated in [8] that careful selection of the isosceles triangular features can reduce these 1D coupling elements in $\mathbf{C}$. Specifically, for PCSELs featuring SIT structures with a base of $\sqrt{2}a/2$ and a height of $3\sqrt{2}a/4$, the submatrix $\mathbf{C}_{1D}$ vanishes entirely. On the other hand, $\Im\Omega_{\mathbf{C}}$ for the PCSELs with the vertical structure [7] considered in this work is small. While this reduces the lasing threshold, it also hinders the achievement of the desired steep slopes in the power-current characteristics during current-tuning calculations.
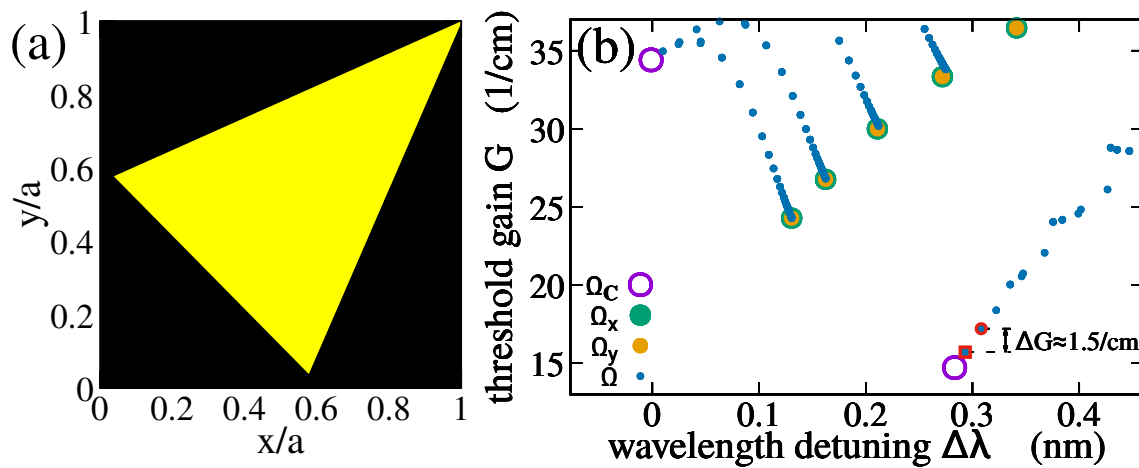

Figure 3: Same as in Fig. 1 for a PCSEL with a SIT-defined PC.

First, we consider a SIT with the base $0.76a$ and the base angle of $68.758°$ (see Fig.3(a)), which does not completely nullify $\mathbf{C}_{1D}$ but effectively reduces the 1D-coupling within $\mathbf{C}$ to a level comparable with its other elements, while maintaining significant $2\Im\Omega_{\mathbf{C}0} = 14.7$ cm^{-1}. Comparing panels (b) of Figs. 1 and 3, calculated with the same PCSEL structure but different PC features, shows that the SIT-based PCSEL yields a slightly smaller G for the fundamental mode, a 20-fold increase in the gain gap ΔG to the first higher-order mode, and a fivefold increase in the gap to the major 1D-modes, clustered at the green/orange bullets in these diagrams. For moderate $\Delta G \approx 1.5$ cm^{-1}, simulations predict single-mode lasing over wide injected current ranges, even without additional structural optimization of the PCSEL.

The dynamics observed during parameter-tuning simulations of the SIT-based PCSEL structure are shown in Fig. 4. Aside from the PC feature, all parameters and the calculation procedure were identical to those in the RIT-based PCSEL case shown in Fig. 2. Since $\Im\Omega$ of the fundamental mode is slightly lower in the SIT-based structure (cf. panels (b) of Figs. 1 and 3), this configuration has a lower threshold
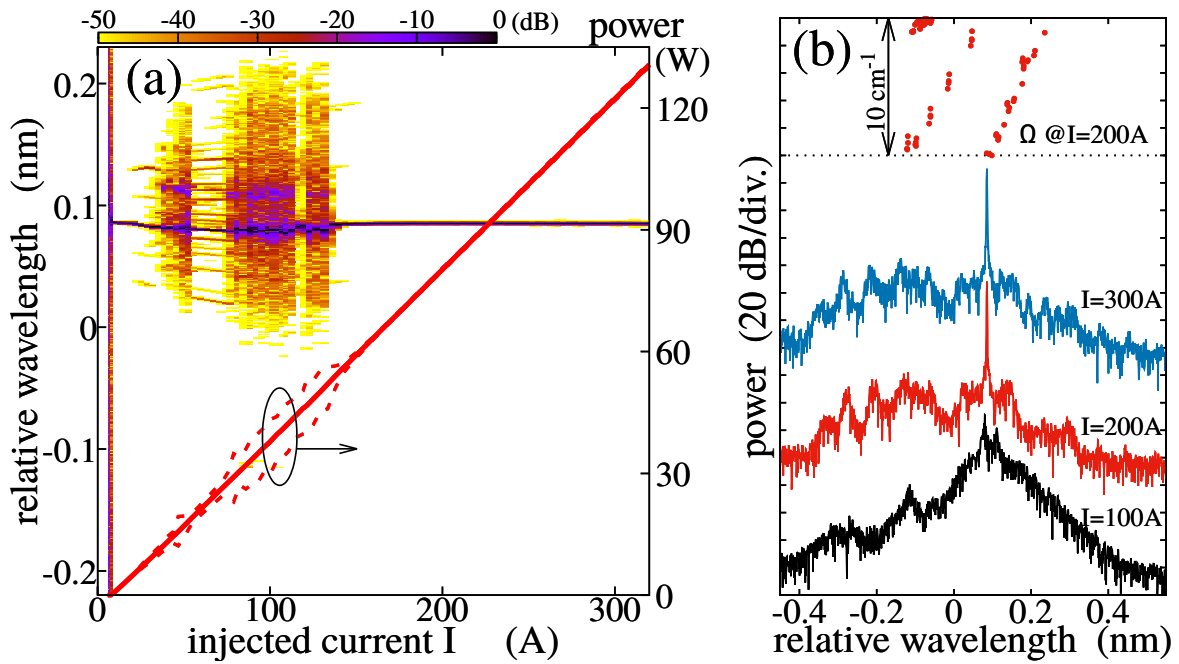
Figure 4: Same as in Fig. 2 for a PCSEL with a SIT-defined PC.

current, reduced carrier density, and a smaller $\Delta_n(N)$-induced blue shift of the lasing wavelength in the hot-cavity PCSEL compared to the RIT-based structure. At higher currents, the emitted power in both cases is nearly identical (compare the red current-power characteristic lines in panel (a) of Figs. 2 and 4). However, the SIT-based structure demonstrates a clear advantage: extended intervals of bias current in which the PCSEL maintains single-mode emission, with all other modes suppressed by at least 50 dB. This single-mode operation occurs near the lasing threshold and at currents above 140 A. Spectra for these single-mode regimes at $I = 200$ and 300 A are shown by the red and blue curves in Fig. 4(b). For intermediate currents ($I \in [20, 140]$A), the simulations reveal irregular multimode lasing. This regime is characterized by broad spectra and visible intensity fluctuations, as indicated by the dark lines in the color-coded spectra, the separation of dashed red lines in panel (a), and the black-line spectra for $I = 100$ A in Fig. 4(b). Notably, the substantial separation of major higher-order modes in SIT-based PCSELs, see, e.g., red dots at the top of panel (b), allows distinct mode identification in the optical spectrum, even during multimode operation (see the separate spectral lines for $I < 80$ A in Fig. 4(b)). This separation is not achievable in RIT-based PCSELs, where modes are densely packed.

Enhanced single-mode lasing can be achieved by using modified SIT (MSIT) features with a base of $0.75a$ and base angle $70°$ as considered in [8], optimized to enhance ΔG at the expense of reduced $\Im\Omega_{C0}$. These MSIT features imply $\Delta G = 1.2 \, \text{cm}^{-1}$ for $L_c = 2.5 \, \text{mm}$-PCSELs, though with notable field losses at the PC layer edges, since $2\Im\Omega_{C,0} \approx 7.62 \, \text{cm}^{-1}$ is visibly less than the fundamental mode gain $G \approx 8.5 \, \text{cm}^{-1}$. Output power is lower than in RIT- or SIT-based lasers (cf different lines in Fig. 5(a)) but shows stable operation with minimal power fluctuations and excellent side mode suppression ($\geq 60 \, \text{dB}$ SMS) over most bias currents, see red dots in the same panel. Selected spectra, including one with the reduced SMS at $I = 600$ A are shown in Fig. 5(b). The presence of only a few spectral peaks indicate a perfect suppression of almost all higher order modes.

In conclusion, we have simulated the above-threshold behavior of all-semiconductor $L \geq 2 \, \text{mm}$ PC-SELs using a 2+1 dimensional PDE model based on 3D coupled-wave theory and a diffusive carrier rate equation, enhanced with an inhomogeneous current-spreading model. For a RIT-feature-based
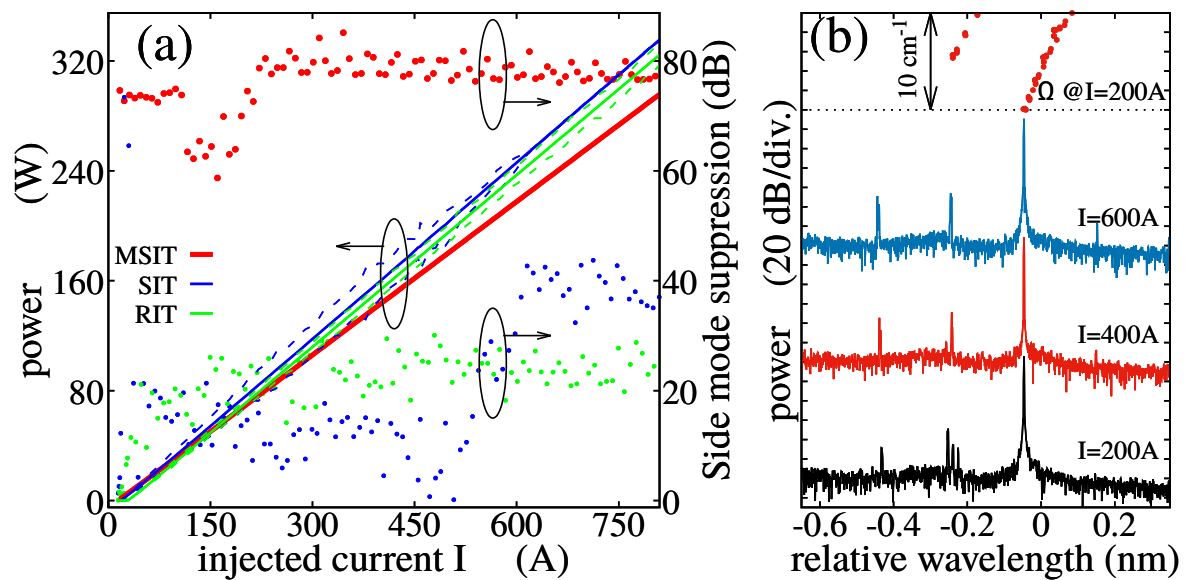
Figure 5: (a): Emission power (lines) and SMS (dots) as functions of bias I in the $L = 3\,\text{mm}$ MSIT-PCSEL with $L_\text{c} = 2.5\,\text{mm}$ (red) and corresponding SIT/RIT-PCSELs (blue/green). (b): Spectra for selected I in MSIT-PCSEL (lines), and wavelengths/damping of the main modes for $I = 200\,\text{A}$ (dots).

PCSEL, our simulations predict multimode operation just above the threshold current. In contrast, simulations of similar SIT-feature-based PCSELs show that the increased mode gain gap ΔG in the cold-cavity design supports single-mode operation over a wider range of bias currents, including high-pumping regions where high-power beams are expected. The simulations employed the basic vertical configuration of the PCSEL [7], where the field is nearly symmetrically redirected to both sides of the PC layer. The incorporation of a DBR, together with precise adjustments to its separation from the active region and PC layer [8], should not only double the emitted power but also facilitate further optimization of $\Im\Omega_{\text{C0}}$ and the fundamental mode gain G, while maintaining a significant mode gain gap ΔG even in large-area all-semiconductor PCSELs.

References

[1] M. Imada, S. Noda, A. Chutinan, et al., "Coherent two-dimensional lasing action in surface-emitting laser with triangular-lattice photonic crystal structure," Appl. Phys. Lett. **75**, pp. 316–318, 1999, doi: 10.1063/1.124361.

[2] S. Noda, K. Kitamura, T. Okino, et al., "Photonic-Crystal Surface-Emitting Lasers: Review and Introduction of Modulated-Photonic Crystals," IEEE J. Sel. Top. Quantum Electron. **23**, art.no. 4900107, 2017, doi: 10.1109/JSTQE.2017.2696883.

[3] T. Inoue, R. Morita, K. Nigo, et al., "Self-evolving photonic crystals for ultrafast photonics," Nat. Communications **14**, art.no. 50, 2023, doi: 10.1038/s41467-022-35599-2.

[4] M. Yoshida, S. Katsuno, T. Inoue, et al., "High-brightness scalable continuous-wave single-mode photonic-crystal laser," Nature **618**, pp. 727–732, 2023, doi: 10.1038/s41586-023-06059-8.

[5] Y. Liang, C. Peng, K. Sakai et al., "Three–dimensional coupled–wave analysis for square–lattice photonic crystal surface emitting lasers with transverse–electric polarization: finite–size effects," Optics Express **20**, pp. 15945–15961, 2012, doi: 10.1364/OE.20.015945.

[6] M. Radziunas, E. Kuhn, H. Wenzel, et al., "Optical mode calculation in large-area photonic crystal surface-emitting lasers," IEEE Photonics J. **16**, art.no. 0601209, 2024, doi: 10.1109/JPHOT.2024.3380532.

[7] H. Wenzel, E. Kuhn, B. King, et al., "Theory of the linewidth-power product of photonic-crystal surface-emitting lasers," arXiv:2402.11246 [physics.optics], 2024, doi: 10.48550/arXiv.2402.11246. To appear in IEEE J. of Quantum Electron.

[8] B. King, H. Wenzel, E. Kuhn, et al., "Design of very-large area photonic crystal surface emitting lasers with an all-semiconductor photonic crystal," Optics Express **32**(25), pp. 44945–44957, 2024, doi: 10.1364/OE.537452.

[9] T. Inoue, R. Morita, M. Yoshida et al., "Comprehensive analysis of photonic-crystal surface-emitting lasers via time-dependent three-dimensional coupled-wave theory," Phys. Rev. B **99**, art.no. 035308, 2019, doi: 10.1103/PhysRevB.99.035308.

[10] T. Inoue, T. Kim, S. Katsuno, et al., "Measurement and numerical analysis of intrinsic spectral linewidths of photonic-crystal surface-emitting lasers," Appl. Phys. Lett. **122**, art.no. 051101, 2023, doi: 10.1063/5.0135042.

[11] M. Radziunas, E. Kuhn, and H. Wenzel, "Solving a spectral problem for large-area photonic crystal surface-emitting lasers," Math. Modelling and Analysis **29**, pp. 575–599, 2014, doi: 10.3846/mma.2024.20496 .

[12] H.-J. Wünsche, M. Radziunas, S. Bauer, et al., "Modeling of mode control and noise in self-pulsating PhaseCOMB lasers," IEEE J. of Sel. Top. Quantum Electron. **9**, pp. 857–864, 2003, doi: 10.1109/JSTQE.2003.818854.

[13] A. Zeghuzi, H.-J. Wünsche, H. Wenzel et al., "Time-dependent simulation of thermal lensing in high-power broad-area semiconductor lasers," IEEE J. Sel. Top. Quantum Electron. **25**, art.no. 1502310, 2019, doi: 10.1109/JSTQE.2019.2925926.

[14] A. Zeghuzi, M. Radziunas, H.-J. Wünsche, et al., "Traveling wave analysis of non-thermal far-field blooming in high-power broad-area lasers," IEEE J. Quantum Electron. **55**, art.no. 2000207, 2019, doi: 10.1109/JQE.2019.2893352.

[15] K. Unger, SSpontane und induzierte Emission in Laserdioden,SZeitschrift für Physik **207**, pp. 322–331, 1967, doi: 10.1007/BF01326347.

[16] M. Radziunas, A. Zeghuzi, J. Fuhrmann, et al., "Efficient coupling of the inhomogeneous current spreading model to the dynamic electro-optical solver for broad-area edge-emitting semiconductor devices," Opt. and Quantum Electron. **49**, art.no. 332, 2017, doi: 10.1007/s11082-017-1168-3.